Computers and Fluids 167 (2018) 33–39

Contents lists available at ScienceDirect

Computers and Fluids

journal homepage: www.elsevier.com/locate/compfluid

Regularized lattice Boltzmann multicomponent models for low capillary and Reynolds microfluidics flows

Andrea Montessori[a,*], Marco Lauricella[b], Michele La Rocca[a], Sauro Succi[b,c], Elad Stolovicki[d], Roy Ziblat[d], David Weitz[d,e]

[a] Department of Engineering, University of Rome "Roma Tre", Via della Vasca Navale 79, Rome 00141, Italy
[b] Istituto per le Applicazioni del Calcolo CNR, Via dei Taurini 19, Rome 00185, Italy
[c] Institute for Applied Computational Science, Harvard John A. Paulson School of Engineering And Applied Sciences, Cambridge, MA 02138, United States
[d] School of Engineering and Applied Sciences, Harvard University, Cambridge, MA, United States
[e] Department of Physics, Harvard University, Cambridge, MA, United States

ARTICLE INFO

Article history:
Received 6 November 2017
Revised 22 February 2018
Accepted 26 February 2018
Available online 27 February 2018

Keywords:
Microfluidics
Lattice Boltzmann Models
Emulsions
Flow Focusing

ABSTRACT

We present a regularized version of the color gradient lattice Boltzmann (LB) scheme for the simulation of droplet formation in microfluidic devices of experimental relevance. The regularized version is shown to provide computationally efficient access to capillary number regimes relevant to droplet generation via microfluidic devices, such as flow-focusers and the more recent microfluidic step emulsifier devices.

1. Introduction

In the last two decades, microfluidic devices have gained a prominent role in several fields of research, from basic fluid dynamics to material science, biomedicine, as well as industrial applications [1–3]. In the early 2000s, several pioneering works showed the potential of such devices for generating droplets at the microscale with unprecedented degree of uniformity and rational design, thereby establishing the basis of the lab-on-a-chip concept [4–7]. Nowadays, many publications show that the drops microfluidics has surged well beyond the proof-of-concept paradigm, proving the viability of the new approach through substantial contributions to chemistry, biology, medicine, 3d-printing, to name but a few [8–12]. Due to their ease of fabrication via soft lithography methods [13,14], microfluidic devices are intensely exploited for the study and manipulation of fluids at the submillimeter length scale. In particular, microfluidic devices have been successfully employed for producing porous scaffolding materials with an accurate control over scaffold specifications, such as pore size, shape, distribution and interconnectivity [15,16].

In such context, droplet generation units are the main components to produce emulsion templating porous materials by means of microfluidic devices. Several droplet-based microfluidic chips include at least one droplet generation unit within different geometries, alongside with droplet splitting/merging units (e.g., flow focusing, coflow, T-, X-, and Y-junctions). Although, experiments have driven many of the advances in the field, many quantities of design interest lie still beyond experimental reach, thereby precluding a complete understanding of the basic physics of droplet generation by experimental means and thus holding back further progress in the operation and optimization of microfluidic devices.

Models and simulations may provide valuable insights into basic microfluidic mechanisms and, more specifically, computational studies can help to elucidate the nature of optimal flow conditions in terms of geometrical and physico–chemical properties, thus facilitating a rational design of the final product.

Over a decade ago, different numerical methods focused on the breakup mechanisms [17,18], characterizing droplet formation in terms of the relevant dimensionless parameters [19,20]. In particular, it was noted that by varying volume flow rates of the dispersed and continuous phases, and therefore changing the Reynolds and capillary numbers, three distinct regimes of formation of droplets can be identified: *squeezing, dripping and jetting*, three regimes which have been found to be consistent with experimental observations [4,21,22]. Among other, the lattice Boltzmann (LB) method has played a major role in the simulation of droplet formation across a wide variety of microfluidic cross-junctions [20,23–26].

* Corresponding author.
E-mail address: andrea.montessori@uniroma3.it (A. Montessori).

https://doi.org/10.1016/j.compfluid.2018.02.029
0045-7930/

The LB method is known to experience stability and efficiency limitations at both low and high viscosities [27]; low viscosities threaten numerical stability, while large ones undermine the very hydrodynamic limit of the LB scheme, due to the onset of strong non-equilibrium effects.

Different strategies can be employed to mitigate the above constraints: the multirelaxation-time (MRT) method [28], and a regularized version (REG) of the standard single-relaxation-time (SRT) LB scheme [29,30], also known as Regularized lattice Bhatnagar–Gross–Krook model, as well as the entropic version of the LB method [31].

In this paper, we investigate and demonstrate the benefits of the regularization procedures, as applied to the color gradient model [32,33], for the simulation of microfluidic devices.

The main idea behind the REG approach is to filter out the non-hydrodynamic modes, also known as ghost-modes, originating from non-equilibrium effects stemming from free molecular motion between two subsequent collisions [30,34–36], which proves particularly useful for microfluidic applications characterized by low capillary numbers.

The paper is organized as follows. In Section 2 the lattice Boltzmann equation with the BGK collisional operator is described, together with the color gradient model and the regularization algorithm for simulating multicomponent fluids . In Section 3 the regularization algorithm is commented and its benefits for LB simulation in microfluidics context are highlighted, while in Section 4 we present the results of flow-focusing simulations in two spatial dimensions, as well as preliminary three-dimensional simulations of the newly proposed step emulsification volcano micro devices. Finally, a summary is provided in Section 5.

2. Methods

The LB immiscible multicomponent model is based on the following lattice Bhatnagar–Gross–Krook (BGK) equation:

$$f_i^k(\vec{x}+\vec{c}_i\Delta t,\, t+\Delta t) = f_i^k(\vec{x},\, t) + \Omega_i^k(f_i^k(\vec{x},\, t)), \tag{1}$$

where f_i^k is the discrete distribution function, representing the probability of finding a particle of the kth component at position $\vec{x}$ and time t with discrete velocity $\vec{c}_i$. The lattice time step is taken equal to 1, and i the index spans the lattice discrete directions $i = 0, \ldots, b$, where $b = 8$ for a two dimensional nine speed lattice (D2Q9). The density ρ^k of the kth fluid component is given by the zeroth order moment of the distribution functions

$$\rho^k(\vec{x},\, t) = \sum_i f_i^k(\vec{x},\, t), \tag{2}$$

while the total momentum $\rho\vec{u}$ is defined by the first order moment:

$$\rho\vec{u} = \sum_i \sum_k f_i^k(\vec{x},\, t)\vec{c}_i. \tag{3}$$

The collision operator Ω_i^k results from the combination of three sub-operators, namely [33,37]

$$\Omega_i^k = \left(\Omega_i^k\right)^{(3)}\left[\left(\Omega_i^k\right)^{(1)} + \left(\Omega_i^k\right)^{(2)}\right]. \tag{4}$$

Here, $\left(\Omega_i^k\right)^{(1)}$ is the standard BGK operator for the kth component, accounting for relaxation towards a local equilibrium

$$\left(\Omega_i^k\right)^{(1)} f_i^k(\vec{x},\, t) = f_i^k(\vec{x},\, t) - \omega_k\left(f_i^k(\vec{x},\, t) - f_i^{k,eq}(\vec{x},\, t)\right), \tag{5}$$

where ω_k is the relaxation rate, and $f_i^{k,eq}(\vec{x},\, t)$ denotes local equilibria, defined by

$$f_i^{k,eq}(\vec{x},\, t) = \rho^k\left[\phi_i^k + w_i\left(\frac{\vec{c}_i\cdot\vec{u}}{c_s^2} + \frac{(\vec{c}_i\cdot\vec{u})^2}{2c_s^4} - \frac{(\vec{u})^2}{2c_s^2}\right)\right]. \tag{6}$$

Here, w_i are weights of the discrete equilibrium distribution functions, c_s is the lattice sound speed, and ϕ_i^k takes values in D2Q9 lattice

$$\phi_i^k = \begin{cases} \alpha_k, & i = 0, \\ (1-\alpha_k)/5, & i = 1,2,3,4, \\ (1-\alpha_k)/20, & i = 5,6,7,8, \end{cases} \tag{7}$$

where we number $i = 1,2,3,4$ the nearest-neighbor lattice displacements, and $i = 5,6,7,8$ the diagonal ones. In the above expression, α_k is a free parameter, modulating the density ratio γ_k of the kth component with respect to the others [38], as well as tuning its relative pressure

$$p^k = \frac{3\rho^k(1-\alpha_k)}{5}. \tag{8}$$

In this work, $\alpha_k = 4/9$ for both components, so that both components have the same density and speed of sound $c_s = 1/\sqrt{3}$.

In this model, $\left(\Omega_i^k\right)^{(2)}$ is a perturbation operator, modeling the surface tension of the kth component. Denoting by $\vec{F}$ the color gradient in terms of the color difference (see below), this term reads

$$\left(\Omega_i^k\right)^{(2)} f_i^k(\vec{x},\, t) = f_i^k(\vec{x},\, t) + \frac{A_k}{2}|\vec{F}|\left[w_i\frac{(\vec{F}\cdot\vec{c}_i)^2}{|\vec{F}|^2} - B_i\right], \tag{9}$$

with the free parameters A_k modeling the surface tension, and B_k a parameter depending on the chosen lattice [38,39]. The above operator models the surface tension, but it does not guarantee the immiscibility between different components. In order to minimize the mixing of the fluids, a recoloring operator $\left(\Omega_i^k\right)^{(3)}$ is introduced. Following the approach in Ref. [38], being ζ and ξ two immiscible fluids, the recoloring operators for the two fluids read as follows

$$\begin{aligned} \left(\Omega_i^\zeta\right)^{(3)} &= \frac{\rho^\zeta}{\rho}f_i + \beta\frac{\rho^\zeta\rho^\xi}{\rho^2}\cos(\phi_i)\sum_{k=\zeta,\xi} f_i^{k,eq}(\rho^k, 0) \\ \left(\Omega_i^\xi\right)^{(3)} &= \frac{\rho^\xi}{\rho}f_i - \beta\frac{\rho^\zeta\rho^\xi}{\rho^2}\cos(\phi_i)\sum_{k=\zeta,\xi} f_i^{k,eq}(\rho^k, 0) \end{aligned} \tag{10}$$

where β is a free parameter and $\cos(\phi_i)$ is the cosine of the angle between the color gradient $\vec{F}$ and the lattice direction $\vec{c}_i$. It is worth mentioning that, in this work, we implemented the color gradient as:

$$\nabla(\rho_\zeta - \rho_\xi)/(\rho_\zeta + \rho_\xi) \tag{11}$$

Note that $f_i^{k,eq}(\rho^k, 0)$ stands for the set of equilibrium distributions of kth fluid evaluated setting the macroscopic velocity to zero. In the above equation, $f_i = \sum_k f_i^k$. The LB color gradient model has been enriched with the so called regularization procedure [29,34,36], namely a discrete Hermite projection of the post-collisional set of distribution functions onto a proper set of Hermite basis. The main idea is to introduce a set of pre-collision distribution functions which are defined only in terms of the macroscopic hydrodynamic moments. All the higher-order non-equilibrium information, often referred to as *ghosts* [28], is discarded.In equations, the regularized LB reads as follows:

$$f_i^k(x_i + c_i\Delta t, t+\Delta t) = \mathcal{R}f_i^{k,neq}(x,t) \equiv f_i^{k,eq} - \Delta t\omega_k(f_i^{k,reg} - f_i^{k,eq}) \tag{12}$$

where $f_i^{k,reg}$ is the hydrodynamic component of the full distribution f_i^k (see [29]) for the kth color, and $\mathcal{R}$ is the regularization operator. The above equation shows that the post-collision distribution, of a 4th-order isotropic lattice, is defined only in terms of the conserved and the transport hydrodynamic modes, namely density ρ, current $\rho\vec{u}$ and momentum–flux tensor $\mathbf{\Pi} = \sum_i f_i\vec{c}_i\vec{c}_i$.

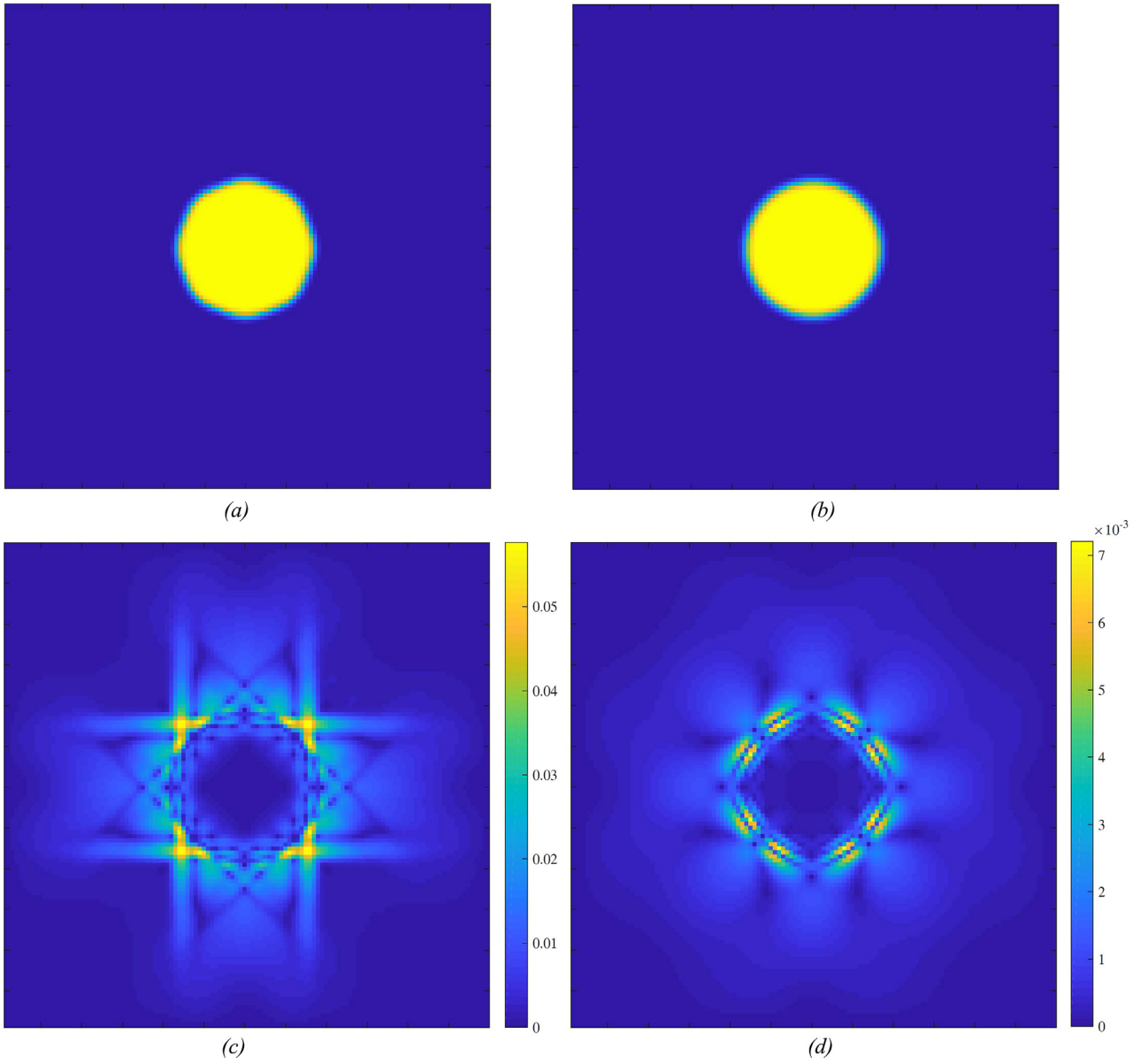

Fig. 1. (a) and (b); density field of a resting droplet immersed in a second component : (a) LBGK (b) Regularized LBGK. The relaxation times of the blue and yellow component were set, respectively, to 1 and 5 ($\nu_B \sim 0.167$, $\nu_Y \sim 1.5$). (c) and (d) velocity field (spurious currents) around the resting droplets for the non regularized (c) and regularized (d) case. It is evident that, for high viscosity values of the dispersed phase, a reduction of isotropy emerges that reflects into a non spherical shape of the resting droplet. An inspection of the flow field highlights that the droplet anisotropy is basically driven by a non-physical flow field around the droplet which is, in turn, caused by the presence of the ghost modes which are excited in the under-relaxed regime ($1/\omega > 1$). As one can see, the regularization cures the loss of isotropy in under-relaxed LBGK, by suppressing the non-physical modes, as evidenced by the circular shape of the droplet at rest and by the spurious flow field around the droplet, which is now isotropic and roughly an order of magnitude smaller than in the plain LBGK case. (For interpretation of the references to color in this figure legend, the reader is referred to the web version of this article.)

For the sake of clarity, in the appendix we report a pseudocode illustrating the regularization procedure employed in our simulations, while in the following section we proceed to discuss the motivation for using the regularization procedure in the color gradient mode.

3. Regularized LB multicomponent approach for low capillary and Reynolds microfluidics

The Reynolds and the capillary numbers are defined as follows:

$$Ca = \frac{\rho \nu U}{\sigma}$$
$$Re = \frac{LU}{\nu} \tag{13}$$

where ν is the kinematic viscosity of the fluid, σ is the surface tension and L and U are, the characteristic length and velocity respectively. Microfluidic flows in T-junctions and flow focusing devices are most often characterized by $Re \sim 1$ and $Ca \ll 1$. For a typical droplet of diameter $D = 10^{-4}$ m, moving at a speed $U = 0.01$ m/s the Reynolds and capillary numbers are $Re = 1$ and $Ca = 10^{-4}$, where we have taken the density of water and a surface tension of $\sim 10^{-3}$ N/m. The diffuse nature of the fluid-fluid interface in the multicomponent model employed in this work, poses some constraint on the ratio between the characteristic length scale of the problem, namely the droplet diameter D, and the width of the diffuse interface, δ, known as Cahn number $Cn = \delta/D$ [40]. Since the interface width lies on nanometric scales, the Cahn number is usually very small, of the order of 10^{-4} or less. Such scale separation is computationally unfeasible, and LB simulations must typ-

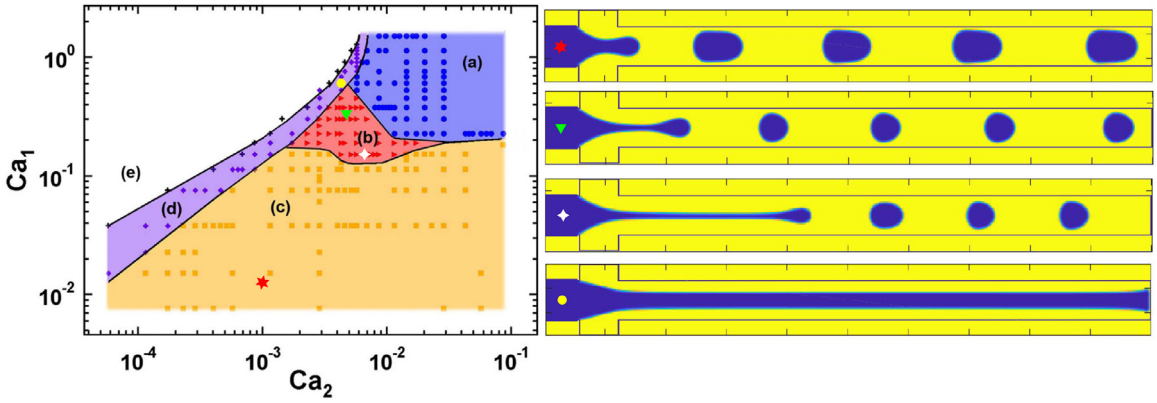

Fig. 2. capillary number-based flow map with flow regimes reproduced by the regularized color gradient model (from the upper left to the lower left panel): Dripping, jetting (second and third) and tubing. The regularized model is capable of accurately predicting the different flow regimes in a microfluidic flow focusing device. The viscosities of the two fluids are $\nu_Y = 0.167$(continuous phase) and $\nu_B \sim 0.5$ (dispersed phase), thus matching the viscosity ratio of the liquids employed in the experiments reported in [41]. (For interpretation of the references to color in this figure legend, the reader is referred to the web version of this article.)

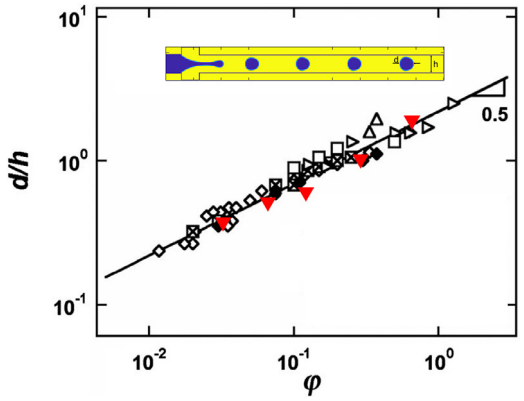

Fig. 3. Normalized droplet diameter d/h vs the flow rate ratio $\phi = Q_B/Q_Y$. Numerical results (Red triangles) are superimposed to the experimental curve of Cubaud and Mason [41]. The diameters collapse on a single master curve, which scales with the flow rate like $Q_B/(2Q_Y)^{0.5}$, as reported in [41].

ically operate at much higher Cahn numbers, between 0.01 and 0.1, implying that the associated inaccuracies must be properly inspected. Given that the diffuse interface is about 5 lattice units, by taking $D_{lb} = 100$ (subscript lb denotes lattice units), we obtain $Cn = 0.05$. Realizing $Re = 1$ with $Cn \sim 0.05$ runs against numerical limitations of the LB method; for instance, by choosing $U_{lb} = 0.001$ and $\nu_{lb} = 0.1$, one faces two inconveniences: first, very long simulation time due to the small velocities, ($U_{lb} = 0.001$ means thousands lattice time steps to cover one lattice spacing), second, a low signal/noise ratio due to spurious currents. The alternative is to raise both the velocity and the viscosity, say $U_{lb} = 0.01$ and $\nu_{lb} = 1$; however, this implies large values of the relaxation time τ, triggering correspondingly large non-equilibrium effects and resulting ghost currents. This is where the benefits of the regularization technique prove key: by filtering out the ghost currents, the Regularized LB can operate at higher values of the droplet speed without incurring into spurious currents and anomalous ghost effects [35].

4. Results

In the following, we present two preliminary applications of the proposed scheme, namely the simulation of droplet formation in standard flow-focusing microfluidic devices and to the recently proposed “volcano” devices [42].

4.1. Flow-focusing devices

We performed simulations of resting droplets of component one (colored as yellow in Fig. 1) immersed in a second component (blue in Fig. 1) with same densities and different viscosities. The size of the domain is 128×128 and the droplet diameter is 30 lattice units The relaxation times of the blue and yellow components were set to 1 and 5 ($\nu_B \sim 0.167$, $\nu_Y \sim 1.5$), respectively. It is worth to highlight that, for high viscosity values of the dispersed phase, sizeable non-isotropic effects arise, resulting in a non-spherical shape of the rest droplet. A more detailed inspection of the flow field shows that the droplet anisotropy is basically driven by a non-physical flow field around the droplet, caused by the presence of the ghost modes. The ghost modes are excited whenever under-relaxed ($\tau > 1$) LBGK models are employed [35]. The regularization cures the loss of isotropy in under-relaxed LBGK, by suppressing the non-physical modes as evidenced by the circular shape of the droplet at rest and by the spurious flow field around the droplet (see Fig. 1 left panels) which is isotropic. Further, the maximum value of spurious currents is an order of magnitude smaller than in the plain LBGK case. We then run simulations of a flow focusing device and compared our results with experimental data available in literature. The simulated device consists of four microchannels with square cross sections of identical width $h = 100$ μm that intersect at right angles, forming a cross channel. The height of the channel is discretized with 30 lattice units so that $\Delta x = 3$ μm. As per the boundary conditions, we imposed uniform velocity profiles at the three inlets of the device by using the bounce-back rule with the momentum correction, as introduced by Bouzidi et al. [43], while a zero gradient approximation has been employed at the outlet by copying the set of distribution functions from in the bulk to the buffer nodes [44]. At the solid walls, the mid-grid bounceback rule has been implemented, so as to mimic a no-slip condition at the wall [44]. Wetting conditions have been implemented by setting two density values, one for each components, at the wall nodes. The contact angle can thus be analytically determined via the following formula [45]:

$$\theta = acos\left(\frac{\rho_{w\zeta} - \rho_{w\xi}}{\rho}\right) \tag{14}$$

For the flow focusing simulations we set $\theta \sim 130°$ by imposing $\frac{\rho_{w\zeta} - \rho_{w\xi}}{\rho} = 0.65$, being $\rho_{w\zeta}$ and $\rho_{w\xi}$ the density values of the two components at the wall nodes.

The viscosities of the two fluids are $\nu_Y = 0.167$(continuous phase) and $\nu_B \sim 0.5$ (dispersed phase), thus matching the viscosity ratio of the liquids employed in the experiments of Ref. [41].

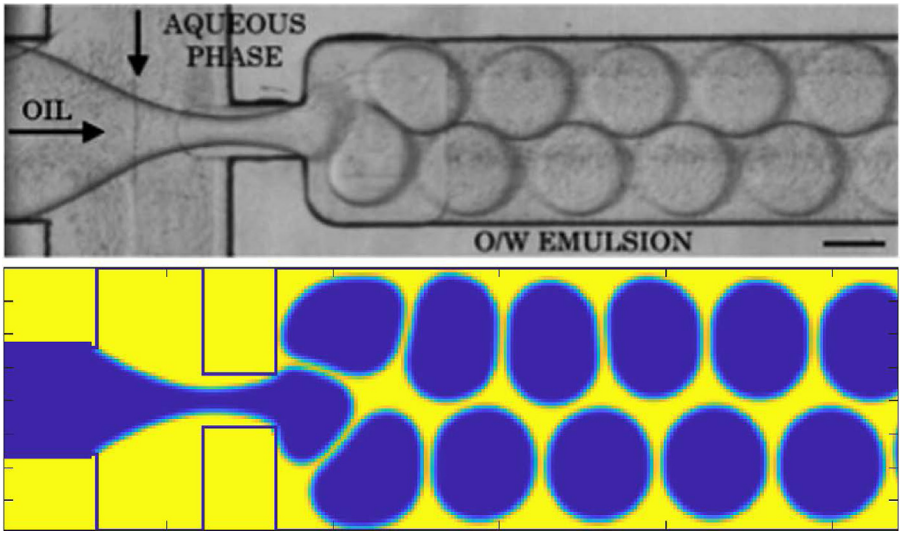

Fig. 4. Prospective application of regularized color gradient model augmented with arrested coalescence algorithm. The model allows for stable simulation of mono-disperse droplets. This opens the way to the simulation of mono-dispersed oil–water emulsions. Future applications of this model will allow to identify optimal operational regimes, capable of delivering droplet configurations of high regularity, both in size and connectivity. Upper panel containing the experimental data is reported from Ref. [15]. (For interpretation of the references to color in this figure legend, the reader is referred to the web version of this article.)

Even in this case, the relaxation time of the dispersed phase (blue in Fig. 2) is greater than one, providing an out of equilibrium regime as in the previous case. In Fig. 2 we report the capillary number-based flow map with flow regimes observed by Cubaud and Mason [41]. The two capillary numbers are defined as follow, $Ca_1 = \mu_1 U_{1,in}/\sigma$ and $Ca_2 = 2\mu_2 U_{2,in}/\sigma$, Where , μ_1 and μ_2 are the dynamic viscosities of the two components, $U_{1,\,in}$ is the inlet velocity of the dispersed component while $U_{2,\,in}$ is the inlet velocity of the continuous component. Finally, σ is the surface tension between the two components Here, we assume that the dynamics of droplet formation is essentially dominated by the balance of tangential shear stresses and capillary tension (i.e. capillary number) in line with several works in literature [1,7,19,46]. As a consequence, the capillary numbers of the two components is used to discern several flow regimes. In Fig. 2, we note a viscous threading regime (labeled (a) in Fig. 2) characterised by the predominant role of the viscous stress over the capillary forces (high values of the capillary numbers Ca_1 and Ca_2). On the contrary, at low $Ca_1 < 10^{-1}$ and $Ca_2 < 10^{-1}$, we observe capillary-dominated flows, providing a dripping of elongated droplets (labeled (c)). In the middle ranges, we note a jetting regime (labeled (b)) characterised by a relatively high viscous force of the first component over a lower capillary number of the second component ($10^{-2} > Ca_2 > 10^{-3}$). Further, we note an intermediate region in the diagram phase describing a tubing regime (labeled (d)), which is characterised by the high capillary force of the second component($Ca_2 < 10^{-2}$) over a halfway behavior of the first component ($Ca_1 \approx 10^{-1}$). The regularized color gradient is clearly able to reproduce the different flow regimes in such microfluidic flow-focusing device, correctly predicting dripping, jetting and tubing flow configurations at different capillary numbers. Next, we computed the normalized droplet diameter d/h, being h the height of the microfluidic channel, versus the flow rate ratio (Q_B/Q_Y, being Q_B and Q_Y the flow rate of the dispersed and continuous component, respectively) and compare with experimental data. The numerical results, in agreement with Ref. [41], collapse on a single master curve, which scales with the flow rate like $Q_B/(2Q_Y)^{0.5}$ (see Fig. 3). As a prospective application, the regularized approach was used to simulate an oil/water emulsion in a flow-focusing device. The use of the regularization has proven to be instrumental to run the flow focusing , due to the high viscosity values of the components employed in the simulations. Indeed, without regularization, unphysical behaviors in the density and velocity fields occur due to the large values of the relaxation frequency, which may eventually drive the simulation unstable. Thus, in view of very refined simulation, the regularization will offer a very easy and efficient way to handle spurious effects coming from the under-relaxation of the distribution functions in the collision processes. In order to obtain a mono-dispersed emulsion, the regularized color gradient approach has been augmented with an algorithm aimed at suppressing coalescence between the droplets of the dispersed phase (oil) (see next subsection for details). The results show that the model allows for stable simulation of mono-disperse droplets, well reproducing the experimental data (see upper panel of Fig. 4). This opens the way to the simulation of mono-dispersed oil–water emulsions. Future applications of this model will allow to identify optimal operational regimes capable of delivering droplet configurations of high regularity, both in size and connectivity, which are of major interest for biomedical and tissue engineering applications.

4.2. Microfluidic step emulsifier (volcanos)

As a further application, we report some preliminary simulations of a new class of step emulsification devices, called volcano [42], which are based on the idea of preventing the obstruction of the nozzles from the droplets via buoyancy effects. These devices are expected to enhance the yield of highly mono-dispersed water/oil or oil/water emulsion, which is highly desirable for most industrial purposes.

The volcano device made from polydimethylsiloxane is used for producing water in oil emulsions. The water flows through the device inlet, and splits into hundreds of step-emulsifier nozzles with rectangular cross section. The device is submerged in a quiescent oil reservoir, each nozzles producing a stream of micron-sized droplets As a preliminary step, we simulated a single-nozzle device, in absence of gravity ($Bo = 0$, being $Bo = \Delta\rho g L^2/\sigma$ the Bond number, namely the ratio between gravitational forces and surface tension). As per the boundary conditions, at the inlet and outlet, we employed the bounce-back rule with the momentum correction and the zero gradient boundary condition, respectively. Periodic boundary conditions have been applied along the crossflow directions. Upon matching the governing dimensionless groups (capil-

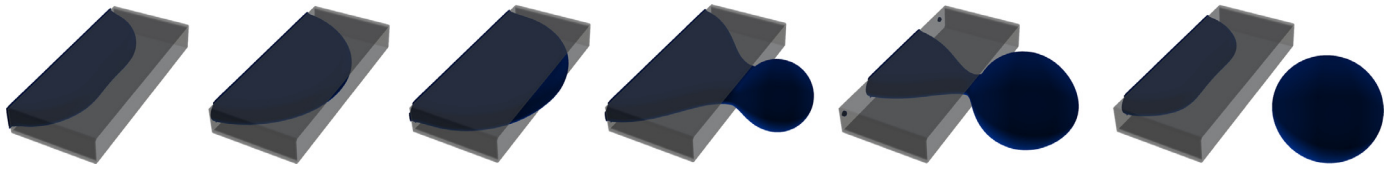

Fig. 5. Droplet breakup sequence. The width of the channel $w = 700$ μm and the height $h = 70$ μm ($h/w = 1/10$), corresponding to capillary number is $Ca = 1.4 \times 10^{-2}$. In this simulation $\Delta x = 7$ μm, the viscosity of the two components $\nu = 0.0167$ and the surface tension of the model is $\sigma = 0.0244$. After the break up, the droplet diameter is $D = 350$ μm, so that $D/h = 5$, in good agreement with the experimental findings on the volcano device ($w/h = 8$, $D/h = 5.8$, $Ca = 10^{-2}$)) [42].

lary and Weber number) and the characteristic geometrical ratio h/w (see the caption of Fig. 5 for the values of the physical parameters), we are able to simulate the droplet break up. After the break up, the droplet diameter is $D \sim 350$ μm, corresponding to $D/h \sim 5$, in good agreement with the experimental findings on the volcano device [42] ($w/h = 8$, $D/h = 5.8$, $Ca = 10^{-2}$). A thorough investigation of the microfluidics of volcano devices is currently underway, and will make the subject of future communications.

5. Summary

Summarizing, we have presented a novel variant of the Lattice Boltzmann method for multiphase flows, based on the regularization of the color-gradient scheme, augmented with a color-swap algorithm to mimic the effect of intermolecular repulsion, so as to tame droplet coalescence. The new scheme has been applied to the simulation of droplet production in flow-focusing microdevices, finding satisfactory agreement with the existing literature, both in terms of predicting the transition from dripping–jetting–tubing regimes, and also in terms of space-time patterns of the droplet configurations in experimental devices. Moreover, we have also presented preliminary three-dimensional simulations of an alternative step emulsifier device, known as volcano device, which is based on the idea of promoting nozzle cleaning via buoyancy effects. If successfully demonstrated, step-emulsifier devices may offer substantial advantages in terms of droplet production rate, degree of mono-dispersity and morphological regularity, versus flow focusing devices.

Acknowledgments

The research leading to these results has received funding from the European Research Council under the European Union's Horizon 2020 Framework Programme (No. FP/2014- 2020)/ERC Grant Agreement No. 739964 ("COPMAT").

Appendix A. Pseudo code of the regularization procedure

Here, a pseudo code of the regularization procedure is reported for the sake of clarity:

for $l \leq b \ \wedge \forall (i,j) \in \mathcal{D}$ **do**
$f_l^{k,neq}(i,j) = f_l^{k,pc}(i,j) - f_l^{k,eq}(i,j)$
end for
for $l \leq b \ \wedge \forall (i,j) \in \mathcal{D}$ **do**
$\Pi_{\alpha,\beta}^{neq,k} = \Pi_{\alpha,\beta}^{neq,k} + (c_{l\alpha}c_{l\beta} - c_s^2\delta_{\alpha\beta}) f_l^{k,neq}(i,j)$
end for
for $l \leq b \ \wedge \forall (i,j) \in \mathcal{D}$ **do**
$f_l^{k,reg}(i,j) = f_l^{k,eq}(i,j) + \frac{w_l}{2c_s^4}(c_{l\alpha}c_{l\beta} - c_s^2\delta_{\alpha\beta})\Pi_{\alpha,\beta}^{neq,k}$
end for

where $f_{l,k}^{pc}(i,j)$ is the set of post-collision distribution functions of the kth component, $f_{l,k}^{neq}(i,j)$ is the non-equilibrium part of $f_{l,k}^{pc}(i,j)$, $p_{\alpha,\beta}^{k}$ are the components of the non-equilibrium part of the momentum flux tensor, $\mathcal{D}$ stands for the fluid domain and $f_{l,k}^{reg}(i,j)$ is the regularized set of post-collision distribution functions. Thus, once the macroscopic moments of both components are computed, it is possible to compute the non equilibrium part of the set of distributions along with the components of the non-equilibrium part of the stress tensor $\Pi^{neq,\,k}$ and then reprojecting the pre-collision set of distribution functions onto a proper Hermite subspace.

Appendix B. Coalescence suppressing algorithm

The coalescence suppressing algorithm is very similar to the one reported in [17]. The main idea is as follows: after the break up, the newly formed droplet changes its color thus becoming immiscible with both the ambient fluid (yellow component in Fig. 4) and the neighboring droplets already present in the main channel. The drop rupture can be detected by monitoring the density profile of the jet of the dispersed phase along the horizontal central axis of the domain. Indeed the droplet separation is signaled by the appearance of a zero in the density profile. Once this occurs, the newly formed droplet is reassigned with a new color, while retaining the same physical properties of the dispersed phase (viscosity and surface tension). It is also important to note that, in order to suppress the mixing between neighboring droplets the surface tension coefficients between the dispersed components must be high enough to guarantee a contact angle of 180° between the droplets. By doing so the coalescence between droplets is completely suppressed. Finally, it is also worth noting that, only five distribution functions are required at each site to prevent coalescence between neighboring droplets, so memory and computing time are virtually independent of the number of droplets to be simulated [17].

References

[1] Anna SL. Droplets and bubbles in microfluidic devices. Annu Rev Fluid Mech 2016;48:285–309.
[2] Vladisavljević GT, Khalid N, Neves MA, Kuroiwa T, Nakajima M, Uemura K, Ichikawa S, Kobayashi I. Industrial lab-on-a-chip: design, applications and scale-up for drug discovery and delivery. Adv Drug Deliv Rev 2013;65(11):1626–63.
[3] Theberge AB, Courtois F, Schaerli Y, Fischlechner M, Abell C, Hollfelder F, Huck WT. Microdroplets in microfluidics: an evolving platform for discoveries in chemistry and biology. Angew Chem Int Ed 2010;49(34):5846–68.
[4] Utada A, Lorenceau E, Link D, Kaplan P, Stone H, Weitz D. Monodisperse double emulsions generated from a microcapillary device. Science 2005;308(5721):537–41.
[5] Anna SL, Bontoux N, Stone HA. Formation of dispersions using "flow focusing" in microchannels. Appl Phys Lett 2003;82(3):364–6.
[6] Gañán Calvo AM, Gordillo JM. Perfectly monodisperse microbubbling by capillary flow focusing. Phys Rev Lett 2001;87(27):274501.
[7] Thorsen T, Roberts RW, Arnold FH, Quake SR. Dynamic pattern formation in a vesicle-generating microfluidic device. Phys Rev Lett 2001;86(18):4163.
[8] Sackmann EK, Fulton AL, Beebe DJ. The present and future role of microfluidics in biomedical research. Nature 2014;507(7491):181.
[9] Rodríguez-Rodríguez J, Sevilla A, Martínez-Bazán C, Gordillo JM. Generation of microbubbles with applications to industry and medicine. Annu Rev Fluid Mech 2015;47:405–29.
[10] Elvira KS, i Solvas XC, Wootton RC, et al. The past, present and potential for microfluidic reactor technology in chemical synthesis. Nat Chem 2013;5(11):905–15.
[11] Mazutis L, Gilbert J, Ung WL, Weitz DA, Griffiths AD, Heyman JA. Single-cell analysis and sorting using droplet-based microfluidics. Nat Protoc 2013;8(5):870–91.

[12] Bhattacharjee N, Urrios A, Kang S, Folch A. The upcoming 3d-printing revolution in microfluidics. Lab Chip 2016;16(10):1720–42.
[13] McDonald J, Duffy D, Anderson J, Chiu D, Wu H, Schueller O, Whitesides G. Fabrication of microfluidic systems in poly (dimethylsiloxane). Electrophoresis 2000;21(1):27–40.
[14] Whitesides GM, Stroock AD. Flexible methods for microfluidics. Phys Today 2001;54(6):42–8.
[15] Costantini M, Colosi C, Guzowski J, Barbetta A, Jaroszewicz J, Święszkowski W, Dentini M, Garstecki P. Highly ordered and tunable polyhipes by using microfluidics. J Mater Chem B 2014;2(16):2290–300.
[16] Oh BH, Bismarck A, Chan-Park MB. Injectable, interconnected, high-porosity macroporous biocompatible gelatin scaffolds made by surfactant-free emulsion templating. Macromol Rapid Commun 2015;36(4):364–72.
[17] Dupin MM, Halliday I, Care CM. Simulation of a microfluidic flow-focusing device. Phys Rev E 2006;73(5):055701.
[18] De Menech M. Modeling of droplet breakup in a microfluidic t-shaped junction with a phase-field model. Phys Rev E 2006;73(3):031505.
[19] De Menech M, Garstecki P, Jousse F, Stone H. Transition from squeezing to dripping in a microfluidic t-shaped junction. J Fluid Mech 2008;595:141–61.
[20] Liu H, Zhang Y. Droplet formation in microfluidic cross-junctions. Phys Fluids 2011;23(8):082101.
[21] Garstecki P, Fuerstman MJ, Stone HA, Whitesides GM. Formation of droplets and bubbles in a microfluidic t-junction-scaling and mechanism of break-up. Lab Chip 2006;6(3):437–46.
[22] Utada AS, Fernandez-Nieves A, Stone HA, Weitz DA. Dripping to jetting transitions in coflowing liquid streams. Phys Rev Lett 2007;99(9):094502.
[23] Wang W, Liu Z, Jin Y, Cheng Y. Lbm simulation of droplet formation in micro-channels. Chem Eng J 2011;173(3):828–36.
[24] Falcucci G, Ubertini S, Chiappini D, Succi S. Modern lattice boltzmann methods for multiphase microflows. IMA J Appl Math 2011;76(5):712–25.
[25] Yan Y, Guo D, Wen S. Numerical simulation of junction point pressure during droplet formation in a microfluidic t-junction. Chem Eng Sci 2012;84:591–601.
[26] Gupta A, Sbragaglia M. A lattice boltzmann study of the effects of viscoelasticity on droplet formation in microfluidic cross-junctions. Eur Phys J E 2016;39(1):2.
[27] Aidun CK, Clausen JR. Lattice-boltzmann method for complex flows. Annu Rev Fluid Mech 2010;42:439–72.
[28] Higuera F, Succi S, Benzi R. Lattice gas dynamics with enhanced collisions. EPL (Europhys Lett) 1989;9(4):345.
[29] Zhang R, Shan X, Chen H. Efficient kinetic method for fluid simulation beyond the Navier–Stokes equation. Phys Rev E 2006;74(4):046703.
[30] Latt J, Chopard B. Lattice boltzmann method with regularized pre-collision distribution functions. Math Comput Simul 2006;72(2):165–8.
[31] Ansumali S, Karlin I, Frouzakis CE, Boulouchos K. Entropic lattice boltzmann method for microflows. Physica A 2006;359:289–305.
[32] Gunstensen AK, Rothman DH, Zaleski S, Zanetti G. Lattice boltzmann model of immiscible fluids. Phys Rev A 1991;43(8):4320.
[33] Leclaire S, Reggio M, Trépanier JY. Numerical evaluation of two recoloring operators for an immiscible two-phase flow lattice Boltzmann model. Appl Math Model 2012;36(5):2237–52.
[34] Montessori A, Falcucci G, Prestininzi P, Rocca ML, Succi S. Regularized lattice Bhatnagar–Gross–Krook model for two-and three-dimensional cavity flow simulations. Phys Rev E 2014;89(5):053317.
[35] Montessori A, Prestininzi P, Rocca ML, Succi S. Lattice boltzmann approach for complex nonequilibrium flows. Physical Review E 2015;92(4):043308.
[36] Falcucci G., Montessori A., Succi S.. On the effects of reactant flow rarefaction on heterogeneous catalysis: a regularized lattice Boltzmann study, Communications in Computational Physics. doi: 10.4208/cicp.OA-2016-0250.
[37] Tölke J. Lattice Boltzmann simulations of binary fluid flow through porous media, philosophical transactions of the royal society of london a: mathematical. Phys Eng Sci 2002;360(1792):535–45.
[38] Leclaire S, Reggio M, Trépanier JY. Isotropic color gradient for simulating very high-density ratios with a two-phase flow lattice Boltzmann model. Comput Fluids 2011;48(1):98–112.
[39] Reis T, Phillips T. Lattice boltzmann model for simulating immiscible two-phase flows. J Phys A 2007;40(14):4033.
[40] Cahn JW, Hilliard JE. Free energy of a nonuniform system. i. interfacial free energy. J Chem Phys 1958;28(2):258–67.
[41] Cubaud T, Mason TG. Capillary threads and viscous droplets in square microchannels. Phys Fluids 2008;20(5):053302.
[42] Stolovicki E., Ziblat R., Weitz D.A. Throughput enhancement of parallel step emulsifier devices by shear-free and efficient nozzle clearance, lab on a chip. URL https://doi.org/10.1039/c7lc01037k.
[43] Bouzidi M, Firdaouss M, Lallemand P. Momentum transfer of a Boltzmann-lattice fluid with boundaries. Phys fluids 2001;13(11):3452–9.
[44] Succi S. The lattice Boltzmann equation: for fluid dynamics and beyond. Oxford University press; 2001.
[45] Huang H, Sukop M, Lu X. Multiphase lattice Boltzmann methods: theory and application. John Wiley & Sons; 2015.
[46] Umbanhowar P, Prasad V, Weitz D. Monodisperse emulsion generation via drop break off in a coflowing stream. Langmuir 2000;16(2):347–51.